Available online at www.sciencedirect.com

ScienceDirect

journal homepage: www.elsevier.com/locate/he

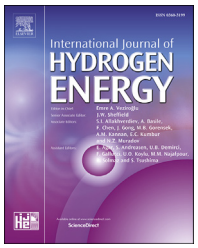

Influence of methanol reformate injection strategy on performance, available exhaust gas enthalpy and emissions of a direct-injection spark ignition engine

A. Poran, L. Tartakovsky *

Technion – Israel Institute of Technology, Technion City, Haifa 3200003, Israel

ARTICLE INFO

Article history:
Received 6 February 2017
Received in revised form
23 April 2017
Accepted 9 May 2017
Available online 26 May 2017

Keywords:
Waste heat recovery
Thermochemical recuperation
Methanol steam reforming
Injection strategy
Engine thermal efficiency
Pollutant emissions

ABSTRACT

This paper presents experimental study results of a direct injection engine fed with methanol steam reforming products and devised to work with a high-pressure thermochemical recuperation system. The influence of injection pressure and timing on heat release rate, fuel mass fraction burned, cycle-to-cycle variation, pollutant emissions, efficiency and exhaust gas energy available for methanol reforming is investigated and analyzed. Effect of injector flow area on the required injection pressure is discussed. End-of-injection (EOI) timing is shown to be the main influencing factor on engine efficiency and pollutant emissions. The obtained results indicate that there is a range of EOI timing where indicated efficiency is almost constant and NO_x emissions drop by a factor of 2.5. Particle number emissions can be reduced in this range by a factor of 4. We showed that engine exhaust gas possesses enough energy to sustain endothermic reforming reactions up to excess air ratio of 2.5.

Introduction

There is a wide agreement that the internal combustion engine (ICE) will remain the main propulsion tool in the foreseen future [1]. Hence, increasing the efficiency of ICEs together with using low carbon intensity fuels are considered nowadays as the most promising ways of air pollution mitigation and crude oil consumption reduction. Methanol and ethanol are low-carbon-intensity fuels widely accepted as promising alternatives to petroleum due to the possibility of their production from various fossil and renewable sources like coal, natural gas and various types of biomass [2–7]. In this article, we will focus on methanol as the primary fuel for an ICE with waste heat recovery (WHR) through high-pressure thermochemical recuperation (TCR).

Since about 1/3 of the energy introduced to an ICE with the fuel is wasted along with the hot exhaust gas, a partial utilization of this energy, also known as waste heat recovery, may result in a substantial improvement of the overall ICE efficiency [8–10]. Turbocharging is the most well-known and widely used WHR method. Another possible way of WHR is based on utilization of the exhaust gas energy to accomplish endothermic reactions of fuel reforming in a specially designed chemical reactor. This method is frequently called

* *Corresponding author.*
E-mail address: tartak@technion.ac.il (L. Tartakovsky).
http://dx.doi.org/10.1016/j.ijhydene.2017.05.056

Nomenclature

Symbols

A	injector flow area
$c_{p,i}$	specific heat at constant pressure of species i
C_D	flow discharge coefficient
$\partial R/\partial X_i$	partial derivative of calculated value R with respect to measured value X_i
δR	uncertainty of calculated parameter R
δX_i	uncertainty interval of variable X_i
ΔH	enthalpy of reaction
ΔT	temperature difference between heat exchanger inlet and outlet
e	energy
E_i	emission of pollutant i
f	methanol conversion fraction
h	enthalpy
$\overline{h}_{av}$	percentage of available enthalpy for reforming
m	mass
$\dot{m}$	mass flow rate
M_C	molecular weight of carbon
M_i	molecular weight of species i
n_i	number of moles of species i
$\dot{n}_i$	molar flow rate of species i
p	pressure
P_i	indicated power
$\overline{q}$	percentage of heat required for reforming from the fuel energy delivered to the engine
Q	heat transfer rate
R	gas constant
T	temperature
V	cylinder volume
V_d	displaced volume
$W_{i,g}$	gross indicated work
$y_{c,fuel}$	fuel's carbon mass fraction
y_i	molar fraction of species i
y_j	molar fraction of gaseous species j containing carbon

Subscripts

a	air
b	burned zone
ch	choked
f	fuel
l	liquid form
M	methanol
s	sensible
u	unburned zone
0	stagnation

Greek symbols

γ	specific heat ratio
η_i	gross indicated thermal efficiency
θ	crank angle whereas 360 deg. is firing top dead center
θ_{0-10}	flame development angle
θ_{90}	CAD of 90% of fuel mass burned
λ	excess air ratio
σ_{IMEP}	IMEP standard deviation

Acronyms

BTDC	before top dead center
BTE	brake thermal efficiency
CAD	crank angle degrees
COV	coefficient of variation in IMEP
DI	direct injection
ED	ethanol decomposition
EEPS	engine exhaust particle sizer
EOI	end of injection
HC	total hydrocarbons
HRR	heat release rate
ICE	internal combustion engine
IMEP	indicated mean effective pressure
IVC	intake valve closing
LHV	lower heating value
MD	methanol decomposition
MSR	methanol steam reforming
PN	particle number concentration
SI	spark ignition
SOI	start of injection
TCR	thermochemical recuperation
TDC	top dead center
WHR	waste heat recovery
WOT	wide-open throttle

thermochemical recuperation (TCR) [11]. TCR has three main advantages over turbocharging. First, utilization of exhaust gas energy is not bounded by the thermodynamic limit of isentropic expansion. Second, the fuel's lower heating value (LHV) is increased as a result of the WHR process (Eqs. (1)–(3)). Third, a mixture of the gaseous reforming products (reformate) usually has a high hydrogen content resulting in higher antiknock quality, wider flammability limits and increased burning velocity of the fuel burned in engine cylinders [12–14]. Thus, TCR enables ICE efficiency improvement not only as a result of waste heat recovery but also because of the great benefits of burning the hydrogen-rich gaseous fuel. Wider flammability limits of the latter enables lean-burn operation with subsequent lower heat transfer and throttling losses. Increased burning velocity results in combustion that is closer to the most efficient constant-volume combustion. Higher antiknock quality opens a possibility of compression ratio increase.

In addition to previously mentioned advantages, methanol and ethanol are also excellent primary fuels for ICE with TCR due to the fact that they can be reformed at relatively low temperatures (around 250–300 °C [4,15]) to produce hydrogen-rich reformate. The latter usually allow utilization of engine exhaust heat without a need in an additional energy source. Widely studied alcohol reforming methods for ICEs include methanol decomposition (MD) – Eq. (1), methanol steam

reforming (MSR) – Eq. (2), and low-temperature ethanol decomposition (ED) – Eq. (3) [8,16–18].

$$CH_3OH_{(g)} \rightarrow CO + 2H_2 \quad \Delta H = 90 \text{ kJ/mol} \tag{1}$$

$$CH_3OH_{(g)} + H_2O_{(g)} \rightarrow CO_2 + 3H_2 \quad \Delta H = 50 \text{ kJ/mol} \tag{2}$$

$$C_2H_5OH_{(g)} \rightarrow CH_4 + CO + H_2 \quad \Delta H = 50 \text{ kJ/mol} \tag{3}$$

Generally, MD may be more beneficial than MSR since the increase in reformate heating value is greater (because the reforming product CO is a fuel – Eq. (1) compared with a diluent gas CO_2 in the case of MSR – Eq. (2), which leads to an increase in the reformate heating value despite some reduction in the hydrogen content), there is no need to carry, preheat and evaporate water in the reformer and the required injection pressure to maintain high power output is lower. The latter is due to the higher energy density of MD products compared with MSR products. However, because of catalyst stability and deactivation problems frequently observed in the methanol decomposition process, the current study focuses on methanol steam reforming – Eq. (2), which is less sensitive to these issues [19,20]. Moreover, the presence of CO_2 in the MSR reformate could be beneficial at high engine loads, because it contributes to a decrease of the in-cylinder temperature and thus leads to a significant reduction of NO_x formation. Nevertheless, in case that the catalyst deactivation and stability problems would be resolved by developing new advanced catalysts, methanol decomposition may still become the advantageous reforming option in the future [21].

The concept of methanol reforming in an ICE with TCR is not new and has been thoroughly investigated since the 1970's. Pettersson and Sjostrom [22] overviewed a progress achieved in this field in their work published in 1991. The studies completed in this period reported on up to 40% improvement in brake thermal efficiency (BTE) compared with gasoline counterpart, but have also identified serious drawbacks of this approach [22]. The main problems that were reported include catalyst deactivation due to coke formation, uncontrolled combustion, cold start and transient behavior issues, and engine maximal power reduction as a result of lower volumetric efficiency. The latter is a consequence of the reformate supply method when the gaseous reforming products were fumigated into the intake system thus reducing the partial pressure of the air in the intake manifold. The absence of charge cooling due to liquid fuel evaporation was an additional factor that led to a lower mass of fresh air introduced to engine cylinder compared with the case of liquid fuel feeding.

More recent studies, which mainly dealt with H_2-ICEs, overcame the issues of power loss and uncontrolled combustion by direct injection (DI) of hydrogen and reported on a high-efficiency low emission hydrogen-fueled ICE [23]. Some researchers studied the influence of hydrogen adding on performance and emissions of SI engines fueled with various primary fuels [12,24]. Hagos et al. [25,26] studied a DI SI engine fueled with syngas ($H_2 + CO$) derived by biomass gasification. They achieved a reduction in CO and HC emissions, but reported on an increase in NO_x emissions at higher loads. In their recent study, Hagos et al. investigated influence of start of injection timing on performance and emissions of a DI SI engine fueled with syngas augmented by 20% of methane [27]. He et al. [28] demonstrated in their research that syngas burning in ICE leads to increase in free radicals concentrations and hence improves the combustion process. A number of studies were devoted to investigation of fundamental combustion properties of various hydrogen-containing fuel–air mixtures [14,29,30]. No published studies are available about the influence of injection strategies on the performance of a DI engine fueled with methanol reforming products mainly consisting of H_2 and CO_2. Li et al. [31] as well as Shimada and Ishikawa [32] studied onboard reforming of hydrous ethanol with reformate supply to the intake manifold. In both works, the authors reported on engine efficiency improvement together with a substantial decrease in emissions of gaseous pollutants NO_x, CO and THC. To prevent engine power loss because of the reformate supply to the intake manifold, in both works [31,32] unreformed ethanol was burned in addition to reformate at high loads. This strategy is also useful in solving the cold start and transient behavior problems. Other approaches recently suggested to overcome these drawbacks of TCR are integration of the reforming system in an electric-hybrid vehicle and using a small on-board pressurized vessel with reformate for start-up purposes [26,33]. Yoon et al. [34] devoted their research to the investigation of design limitations of a reformer intended for the steam reforming of methanol. In the previous study [35] we suggested applying the DI concept to maintain engine's maximal power and prevent uncontrolled combustion but noticed that if reforming is carried out at atmospheric pressure, a significant fraction of the engine power would be required to compress the gaseous reformate prior to its injection. To eliminate this shortcoming while keeping the advantageous direct injection approach, we suggested the concept of high-pressure TCR. In our approach we used the findings of Peppley et al. [36] who tested a commercial $CuO/ZnO/Al_2O_3$ catalyst in MSR reactions up to a pressure of 40 bar and didn't find any significant deactivation problem.

In the previously conducted simulation of ICE with high-pressure TCR system based on methanol steam reforming, we showed a possibility of BTE improvement at rated power regime by 14% compared to the gasoline-fed counterpart [35]. Previous simulations also showed that engine feeding with MSR reformate leads to reduced pollutant emissions compared to gasoline [33]. In the first part of the work reported in this article, we experimentally proved the findings of the previous simulations for constant reformate injection pressure and fuel injection timing at various engine loads. We assessed the available enthalpy of the exhaust gas needed for fuel reforming and analyzed the influence of the injection timing on this important parameter. Then, we studied the influence of the injection pressure and timing on the engine efficiency and pollutants formation at a constant engine operating mode. The latter investigation was essential because of a need to find the lowest injection pressure, which allows efficient operation of a DI SI ICE fed by MSR reforming products, as a milestone on the way towards creating a complete system of ICE with high-pressure TCR.

Methodology

Experimental setup

The experimental setup was developed based on a spark ignition (SI) single-cylinder carburetor gasoline-fed engine of a generator set. The engine was rebuilt to enable direct-injection of various gaseous fuels, like MSR and ED reformates, methane etc. while keeping its baseline capability of gasoline-fed operation. The engine is a part of a laboratory experimental setup with a high-pressure TCR system. A schematic layout of the experimental setup is shown in Fig. 1.

The baseline laboratory engine was a Robin-EY20-3 single-cylinder, 4-stroke, SI, air-cooled side-valve ICE (1) coupled with a 2.2 kW 230 V AC Sincro GP100 generator (13). The reason for the selection of this engine as a basis for the first prototype of a DI MSR-fed ICE was the extra space available in the cylinder head that enabled a relatively easy installation of a new in-house developed gas-DI injector and a pressure transducer. Table 1 shows the main specifications of the baseline engine.

The original ignition system of the Robin EY-20 engine was replaced by a Denso IWF 24 Iridium spark plug (3) and an AEM 30-2853 coil (2) to prevent pre-ignition and allow ignition timing variation.

A dSPACE DS 1104 controller (9) connected to a computer (34) was used for engine control and data acquisition. The equipment for combustion process measurement and analysis included a Kistler 6061B water-cooled pressure transducer (5), a Kistler 5018 charge amplifier (6) and a Kistler crankshaft encoder 2613B (7) with a resolution of 0.5° mounted on the free end of the generator shaft.

Table 1 – Robin EY-20 engine – main parameters.

Bore × Stroke, mm	67 × 52
Displacement, cm^3	183
Compression ratio	6.3
Power, kW @ speed, rpm	2.2 @ 3000
Continues BMEP@3000 rpm, bar	4.8
Gasoline feed system	Carburetor

In the case of gasoline-fed operation, the desired engine speed was controlled by varying the spring load of the governor with aid of a linear actuator (12). When the ICE was fed with MSR reformate, it was run at the wide-open-throttle (WOT) and thus engine speed was governed by varying the load and the amount of injected fuel. Engine load was controlled via a variable transformer and resistors that were connected to the generator.

A Bronkhorst F111-AI-70K-ABD-55-E mass flowmeter (24) and FLUIDAT software were used to measure MSR mass flow rate based on the constant pressure specific heat of the reformate. Gasoline mass consumption was measured by GF-12 K digital scales of A&D Ltd (22).

In these experiments MSR reformate containing 75% H_2 and 25% CO_2 (on a molar basis) was supplied to the engine from premixed compressed gas vessels (28). The mixture composition accuracy was ±1% of the lowest concentration species provided by a gas mixtures supplier. A pressure regulator (27) was used to set the desired injection pressure.

Measurement of CO_2, CO, total hydrocarbons (HC) and NO_x concentrations was performed with a California Analytical Instrument (CAI) 600 series NDIR CO/CO_2 analyzer, CAI 600 series FID HC analyzer and a 200EH chemiluminescent NO_x

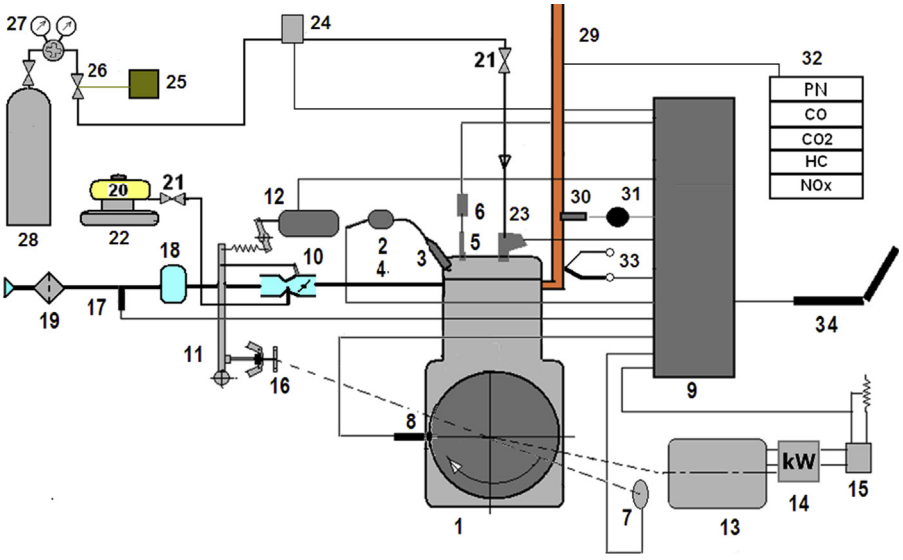

Fig. 1 – Experimental setup. 1 – Robin EY20-3 single cylinder ICE; 2 – ignition coil; 3 – spark plug; 4 – air intake system; 5 – pressure transducer; 6 – charge amplifier; 7 – crankshaft encoder; 8 – TDC proximity sensor; 9 – data acquisitor and controller; 10 – throttle; 11 – centrifugal speed governor; 12 – linear actuator; 13 – generator; 14 – power gauge 15 – generator load; 16 – crankshaft driven gear of the engine speed governor; 17 – air flow meter; 18 – pressure wave damper; 19 – air filter; 20 – gasoline tank; 21 – valve; 22 – electronic scales; 23 – DI gas injector; 24 – gas flow meter; 25 – hydrogen detector; 26 – emergency self-acting stop cock; 27 – pressure regulator; 28 – gas cylinder; 29 – exhaust line; 30 – O_2 sensor; 31 – air-to-fuel ratio gauge; 32 – exhaust gas analyzers; 33 – thermocouple; 34 – computer.

analyzer (equipped with a thermal converter 501x) of Teledyne Instruments. Sampling for measurements of CO_2, CO and NO_x was carried out from a dried exhaust gas sampling line and for HC measurements – directly from the exhaust line. Particles number concentration (PN) and size distribution were measured with aid of TSI-made Engine Exhaust Particle Sizer (EEPS) of 3090 model (32). The latter enabled measuring emission of particles from 5.6 to 560 nm with particle size resolution of 16 channels per decade (32 total) and time resolution of 10 Hz. TSI-made rotating disk thermodiluter thermal conditioning device 379020A-30 was used for diluting and conditioning the sample in accordance with the requirements of PMP procedure. The sample was heated to 300 °C to eliminate volatiles.

A VA-420 flow sensor of CS Instruments was used to measure the intake air flow. The measurement results were double-checked with aid of a wide-band Lambda sensor kit LC-1 of Innovate Motorsports based on a Bosch LSU 4.2 O_2 sensor (30) and verified using exhaust gas carbon balance calculation.

As mentioned above, for this research a direct gaseous fuel injector was developed in-house. The developed injector was based on a commercially available gasoline DI injector produced by Magneti Marelli (IHP072). The injector was modified to allow higher volumetric flow rates necessary for the case of gaseous hydrogen-rich reformate fuel injection. The injector's flow area was 0.85 mm^2 and its discharge coefficient was in the range of 0.79 ± 0.02. More details regarding the injector design and the development procedure can be found in Ref. [37]. Fig. 2 [38] shows the cylinder head with the installed injector, pressure sensor and spark plug and their relative location.

The relative location of the injector and spark plug was not optimized. The latter task was beyond the scope of this work.

Data processing

This section provides a description of the measured data processing methods that were applied in this study to obtain information necessary for analysis of the experimental results.

Gross indicated mean effective pressure (IMEP) was calculated using Eq. (4):

$$\mathrm{IMEP} = \frac{\int_{V(\theta=180)}^{V(\theta=540)} p\mathrm{d}V}{V_d} = \frac{W_{i,g}}{V_d} \tag{4}$$

where: V_d – displaced volume [m^3]; $V(\theta = 180)$ – cylinder volume at the start of compression stroke [m^3]; $V(\theta = 540)$ – cylinder volume at the end of compression stroke [m^3]; V – instantaneous cylinder volume [m^3]; p – instantaneous in-cylinder pressure [Pa]; $W_{i,g}$ – gross indicated work [J].

IMEP was calculated by integration of measured instantaneous in-cylinder pressure values over the cylinder displaced volume while excluding the intake and the exhaust strokes. The trapezoidal method was used for the numerical integration.

An important parameter crucial for in-depth analysis of ICE combustion process and cycle-to-cycle variability is the coefficient of variation (COV). It is defined as the standard deviation of IMEP divided by the mean IMEP value as shown in (Eq. (5)) [39]:

$$\mathrm{COV} = \frac{\sigma_{\mathrm{IMEP}}}{\mathrm{IMEP}} \tag{5}$$

where: σ_{IMEP} – IMEP standard deviation; IMEP – average IMEP of all considered cycles [Pa].

The COV values were calculated in this work based on measurement of approximately 100 cycles. Indicated thermal efficiency (η_i) was calculated according to Eq. (6):

$$\eta_i = \frac{W_{i,g}}{m_f \cdot LHV_f} \tag{6}$$

where m_f is the fuel mass supplied to the cylinder per cycle ([kg]) and LHV_f is the lower heating value of the fuel [J/kg].

For the case of engine fueled with MSR products, the indicated efficiency was calculated based on the methanol mass that was consumed to produce the reforming products and the methanol LHV (Eq. (7)):

$$\eta_{MSR} = \frac{W_{i,g}}{\frac{n_M \cdot M_M}{n_W \cdot M_W + n_M \cdot M_M} \cdot m_{MSR} \cdot LHV_M} \tag{7}$$

where: m_{MSR} – MSR products mass supplied to the cylinder per

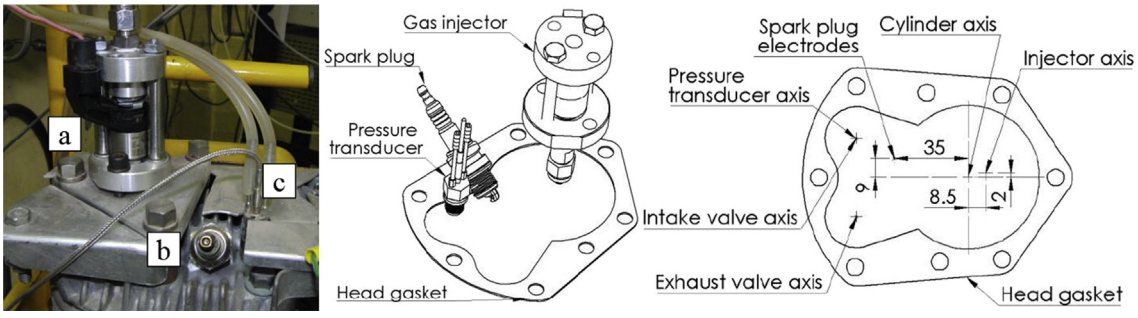

Fig. 2 – On the left, a picture of the gas injector (a) spark plug (b) and pressure transducer (c) as installed on the cylinder head. In the middle, drawing of the same components and the cylinder head gasket with the cylinder head omitted to enable a clear view of the components. On the right, dimensions between the cylinder axis, spark plug electrodes and injection axis are given in mm (the spark plug electrodes and injector nozzle are located 12 mm and 0.3 mm above the gasket plane respectively) [38].

cycle [kg]; n_M – number of methanol moles participating in the MSR reaction [mol]; n_W – number of water moles participating in the MSR reaction [mol]; M_M – molar mass of methanol [kg/mol]; M_W – molar mass of water [kg/mol]; LHV_M– lower heating value of methanol [J/kg].

Mass fraction burned and heat release rate (HRR) were calculated using GT-Power software by processing the measured values of in-cylinder pressure, piston position, injected fuel mass and the amount of fresh air introduced into the cylinder. Pressure pegging was performed using least squares method described in Ref. [40]. Due to the fact that at some engine operating modes gaseous reformate injection started closely after the inlet valve close, in these cases the pressure pegging method was applied for the compression period after the end of injection and before ignition. Moreover, all pegging results were double-checked using another approach where the error between the measured and the simulated pressure values during 40 CAD in the compression stroke was minimized by applying a pressure offset. An advantage of the latter approach is that it uses extra measured values such as fuel mass and fresh air contents in the cylinder. Both methods gave similar results. A two-zone combustion model was used by applying the first law for a control volume for both the burned and the unburned fuel zones – Eqs. (8) and (9) [41]:

$$\frac{d(m_u e_u)}{dt} = -p\frac{dV_u}{dt} - Q_u + \left(\frac{dm_f}{dt}h_f + \frac{dm_a}{dt}h_a\right) + \frac{dm_{f,i}}{dt}h_{f,i} \quad (8)$$

$$\frac{d(m_b e_b)}{dt} = -p\frac{dV_b}{dt} - Q_b - \left(\frac{dm_f}{dt}h_f + \frac{dm_a}{dt}h_a\right) \quad (9)$$

where: m_u – unburned zone mass [kg]; e_u – unburned zone energy [J/kg]; p – in-cylinder pressure [Pa]; V_u – unburned zone volume [m^3]; Q_u – unburned zone heat transfer rate [W]; m_f – fuel mass [kg]; h_f – fuel enthalpy [J/kg]; m_a – air mass [kg]; h_a – air enthalpy [J/kg]; $m_{f,i}$ – injected fuel mass [kg]; $h_{f,i}$ – injected fuel enthalpy [J/kg]; m_b – burned zone mass [kg]; e_b – burned zone energy [J/kg]; V_b – burned zone volume [m^3]; Q_b – burned zone heat transfer rate [W].

In the two-zone model, initially, the entire cylinder charge is located in the unburned zone. After the start of combustion, at any time step, a definite portion of the unburned mixture is being transferred to the burned zone. At each time step, the reacting gases in the burned zone are assumed to be in thermodynamic equilibrium. Based on this assumption, the time-dependent temperature and pressure values are calculated. The amount of unburned mixture that has transferred to the burned zone was calculated to match the measured instantaneous pressure value by an iterative method. To perform the burned mass fraction calculation, additional information was necessary: the residual gas fraction in the cylinder and heat transfer to cylinder walls. Woschni model without swirl or tumble was used to calculate the latter. Measured values of the exhaust gas temperature and the assumption of 100% fuel mass burned were used to set a proper convection heat transfer multiplayer. Residual gas fraction values were calculated by simulating engine operation with GT-Power software while calibrating it to experimental data obtained by us. Flame development angle (θ_{0-10}) and mass fraction burned values were calculated based on the obtained instantaneous values of burned mass. Heat release rate was calculated using the same assumptions, but with a single-zone first law Eq. (10) for control volume [39]:

$$HRR = -p\frac{dV}{d\theta} - Q - \frac{d(m\cdot e_s)}{d\theta} \quad (10)$$

where: V – cylinder volume [m^3]; θ – crank angle [deg]; Q – heat transfer rate [J/deg]; m – in-cylinder mass [kg]; e_s – sensible energy of the cylinder content [J/kg].

Calculation of specific pollutant emissions (in g/kWh) was carried out based on pollutants concentration measurements and carbon balance analysis while using measured fuel flow rate and assuming that lube oil combustion and particulates formation has only minor effect on the carbon balance (Eq. (11)):

$$E_i = \frac{\dot{m}_f \cdot y_{c,fuel} \cdot y_i \cdot M_i}{M_C \cdot \sum y_j \cdot P_i} \quad (11)$$

where: E_i – specific emission of pollutant i [g/kWh]; $\dot{m}_f$ – fuel mass flow rate [g/h]; $y_{c,fuel}$ – fuel's carbon mass fraction; y_i – molar fraction of pollutant i; M_i – molecular weight of pollutant i [kg/mol]; M_C – molecular weight of carbon [kg/mol]; y_j – molar fraction of gaseous carbon-containing species CO, CO_2, HC (calculated as $CH_{1.85}$); P_i – indicated power [kW].

A choked flow equation for ideal gas was used to calculate the influence of injector flow area and injection period on the gaseous fuel flow through the injector [39]:

$$\dot{m}_{ch} = C_D \cdot A \cdot p_0 \sqrt{\frac{\gamma}{R\cdot T_0}}\left(\frac{2}{1+\gamma}\right)^{\frac{\gamma+1}{2(\gamma-1)}} \quad (12)$$

where: $\dot{m}_{ch}$ – choked mass fuel flow rate through the injector [kg/s]; C_D – flow discharge coefficient; A – the injector's reference flow area [m^2]; p_0 – inlet stagnation pressure [Pa]; R – gas constant [J/kg/K]; T_0 – inlet stagnation temperature [K]; γ – specific heat ratio.

The uncertainty of the calculated parameters was evaluated using Eq. (13) [42].

$$\delta R = \left(\sum_{i=1}^{N}\left(\frac{\partial R}{\partial X_i}\delta X_i\right)^2\right)^{1/2} \quad (13)$$

where: δR – uncertainty of calculated parameter R; $\partial R/\partial X_i$ – partial derivative of R with respect to variableX_i; δX_i – uncertainty interval of variable X_i (considering fixed and random errors).

It is known that indicated work calculation is insensitive to random noise and absolute pressure referencing errors, but on the other hand, it is very sensitive to crank phasing errors [43]. Its calculation also involves numerical integration. Thus, indicated work uncertainty was calculated using an approach described by Moffat [42] for computation of uncertainty when using a computer program for results analysis. An angle phase error of ±0.5 CAD was used for this calculation (equal to the encoder resolution). Knowing uncertainty of indicated work calculation is important since it is used later for calculation of indicated efficiency and specific pollutant emissions. Uncertainty values calculated for indicated efficiency and emissions of NO_x, HC, CO and CO_2 are shown as error bars in Figs. 9 and 11–16. The uncertainty was calculated for all these parameters at each studied engine operating mode. However, in some

cases due to the wide range of values that appear in one graph, error bars may not be seen due to the fact that the uncertainty range is small compared to the y-axis scale. In these cases, the uncertainty may be assumed to be as the size of the marker in the plot area. For the readers' convenience, Table 2 summarizes the accuracy of the measured data and the uncertainty values of the calculated parameters.

Available enthalpy of exhaust gas

When considering an onboard fuel reforming system, it is important to make sure that the exhaust gas possesses enough energy to sustain the endothermic reforming reactions. In our previous work [35] we showed that full conversion of methanol is not necessarily beneficial because the non-reformed methanol can be reused relatively easily – Fig. 3. In order to achieve higher flow rate through the injector, cooling of the reformate before its injection is required. On the other hand, the enthalpy of the reformate as it exits the reformer can be utilized to preheat the incoming methanol–water mixture before it enters the reformer. Thus, in our approach we use a heat exchanger to serve both of these purposes (Fig. 3).

At steady-state conditions, the flow rates of the primary fuel that enters the reformer (1), of the gaseous reformate that enters the engine (5) and of the exhaust gas (7) are interrelated. The relationship between (5) and (7) depends on λ. The relationship between (1) and (5) can be expressed by the methanol conversion fraction *f*:

$$f = (\dot{n}_{M,1} - \dot{n}_{M,4})/\dot{n}_{M,1} \tag{14}$$

where $\dot{n}_{M,1}$ is the methanol molar flow rate at the entry to the heat exchanger (1) and $\dot{n}_{M,4}$ is the methanol molar flow rate at the heat exchanger outlet (4) [mol/s].

It is useful to normalize both the heat required for reforming and the exhaust gas available enthalpy by the available enthalpy of the fuel that enters the engine. Thus, the overall fuel flow rate is canceled when dividing and the resulting expressions allow simpler analysis unaffected by the fuel flow rate and hence the engine power. The normalized heat (in %) required for reforming ($\overline{q}$) was calculated according to Eq. (15):

$$\overline{q} = \frac{f\left(h_{CO_2}(T+\Delta T) + 3\cdot h_{H_2}(T+\Delta T)\right) + (1-f)\left(h_{H_2O,l}(T+\Delta T) + h_{M,l}(T+\Delta T)\right) - \left(h_{H_2O,l}(T) + h_{M,l}(T)\right)}{4\cdot f\cdot LHV_f}\cdot 100\% \tag{15}$$

where: $h_i(T)$ – total enthalpy (sum of the enthalpy of formation and the sensible enthalpy) of species *i* at temperature *T* [J/mol]; LHV_f – lower heating value of MSR reformate per mole ($181.37\cdot 10^3$ [J/mol]); ΔT – temperature difference between heat exchanger inlet (1) and outlet (4) [K]. Subscript *l* denotes liquid phase.

The normalized available enthalpy ($\overline{h}_{av}$) was calculated by subtracting the enthalpy of the cold exhaust gas (8) from the enthalpy of the hot exhaust gas (7) and dividing it by the available enthalpy of the fuel entering the engine (5), while

Table 2 – Measuring devices in the experimental setup, their accuracy and uncertainty of calculated parameters.

Device/Parameter	Manufacturer (Accuracy)/Uncertainty
Accuracy of measured parameters	
Crankshaft encoder 2613B	Kistler, (Resolution 0.5° Dynamic accuracy ±0.02° at 10,000 rpm)
Charge Amplifier Type 5018	Kistler, (<±0.3% at 0–60 °C)
Water cooled pressure transducer 6061B	Kistler, (Max. linearity ≤±0.29% FS[a])
Mass flow meter F-111AI-70K-ABD-55-E	Bronkhorst High-Tech B.V., ±(0.5% of MV[a] + 0.1% of FS[a])
Air flow sensor VA420 with integrated measuring unit	CS Instruments GmbH, (±1.5% of MV[a])
Wide-band lambda sensor LC-1 kit	Innovate Motorsports based on Bosch LSU 4.2 O_2 sensor, (at λ = 1: ±0.007; at λ = 1.7: ±0.05)
NO_x analyzer 200EH	Teledyne Instruments, (0.5% of MV[a])
HC analyzer 600 series	California Analytical Instruments, (±0.5% of FS[a])
CO, CO_2 analyzer 600 series	California Analytical Instruments, (±1% of FS[a])
Engine Exhaust Particle Sizer 3090	TSI, NA[a,b]
Rotating Disk Thermodiluter 379020A	TSI, (±10%)
Power gauge (Wattmeter) DW-6060	Lutron Electronics Company, (±1%)
Digital scales GF-12K	A&D Ltd, (±0.1 g)
Maximal uncertainty of calculated parameters, %	
Indicated work	±5%
COV	±4%
Indicated power	±5%

[a] FS – full scale, MV – Measured value, NA – Not available.

[b] In a research conducted by TSI to improve EEPS' PN concentration and size distribution measuring accuracy [44] a new SOOT matrix was developed, and it was found that while using it the EEPS provides PN concentration readings in the range 84%–96% of those obtained with a scanning mobility particle sizer (SMPS) across a wide range of diesel engine operating conditions. The instrument with the same SOOT matrix was applied in our experiments as well.

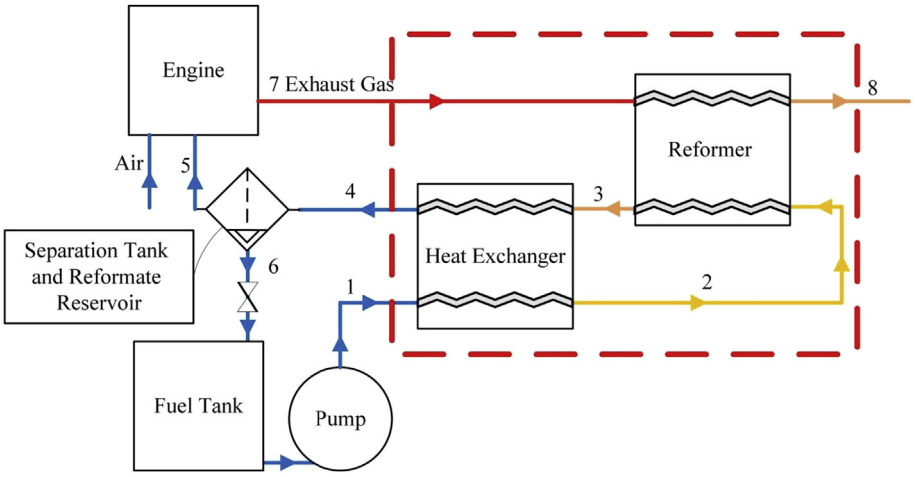

Fig. 3 – Schematic of the considered high-pressure TCR system. 1 – methanol and water mix (1:1 molar ratio) at high pressure; 2 – preheated methanol and water mix; 3 – hot reforming products with residues of unreformed methanol and water; 4 – cooled reforming products with condensed unreformed methanol and water; 5 – cooled gaseous reformate; 6 – condensed unreformed methanol and water; 7 – hot exhaust gas; 8 – cooled exhaust gas.

assuming exhaust gas is an ideal gas and its composition is that of complete combustion products (Eq. (16)):

$$\overline{h}_{av}(\lambda, T_7, T_8) = \frac{\left(1+\lambda\left(\frac{n_a}{n_f}\right)_{st}\right)\left(\sum y_i \int_{T_8}^{T_7} c_{p,i}dT\right)}{LVH_f}\cdot 100\% \qquad (16)$$

where: T_8 – exhaust gas temperature at the reformer inlet (8) – Fig. 3 [K]; T_7 – exhaust gas temperature at the reformer outlet (7) [K]; $\dot{n}_f$ – fuel flow rate at the engine inlet (5) [mol/s]; $\dot{n}_a$ – air molar flow rate [mol/s]; y_i – molar fraction of species i based on complete combustion stoichiometry; $c_{p,i}$ – specific heat of species i at constant pressure [J/mol/K].

Results and discussion

At the first stage of the research, a comparison between engine fueled with MSR reformate and gasoline at constant injection pressure (40 bar) and injection timing (start of injection @ 127 CAD before top dead center – BTDC) was performed. Engine feeding with the MSR reformate enabled unthrottled operation in the entire range of loads. Also, the excess air ratio (λ) that allowed stable engine operation (COV <5% [3]) was much higher than that of gasoline (Fig. 4). This is a result of the high burning velocity and wide flammability limits of the hydrogen-rich reformate that substantially decrease the flame development duration compared to engine fueled with gasoline – Fig. 4.

High burning velocity of the hydrogen-rich reformate enables getting closer to the theoretical Otto cycle. Wide flammability limits of the MSR reformate allow lean-burn operation with the subsequent reduction in throttling and heat transfer losses. In addition, the gaseous MSR reformate reduces the heterogeneity of air–fuel blending. All these, together with the benefits of WHR, led to a substantial improvement in engine efficiency compared to gasoline across the entire range of engine loads (from idle to rated power) (Fig. 5). The lean combustion and CO_2 presence in the MSR reformate reduce the in-cylinder temperature and thus contribute to decrease in NO_x formation. The only source of hydrocarbons formation in case of lean MSR combustion is the lubricant. This fact, together with lean burning result in drastic reduction of CO and HC emissions compared to gasoline.

As seen from Fig. 5, the thermal efficiency of the ICE fueled with MSR products was improved by 18–39% compared to gasoline and emissions of CO, HC and NO_x were reduced by 90–96%, 85–97%, 73–94%, respectively for the specified injection pressure and timing. Even though a possibility of unthrottled operation of ICE fueled with MSR products was demonstrated for the case of onboard methanol reforming, it is important to ensure that the exhaust gas possesses enough available enthalpy to sustain the endothermic reforming reactions. To calculate the heat required for the reforming reactions ($\overline{q}$) and the available enthalpy of the exhaust gas ($\overline{h}_{av}$), Eqs. (15) and (16) were used. Fig. 6 shows the normalized heat required for reforming ($\overline{q}$) as a function of conversion fraction

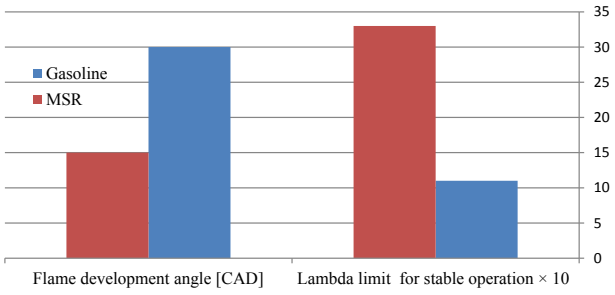

Fig. 4 – Comparison of lambda limit for stable engine operation (COV <5%) and flame development angle between gasoline and MSR products. Engine speed 2800 rpm, SOI 127 CAD BTDC, injection pressure 40 bar.

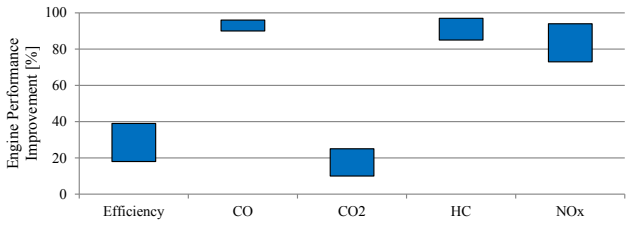

Fig. 5 – Improvement in engine efficiency and pollutant emissions for MSR reformate feeding compared with gasoline. Engine speed 2800 rpm, injection pressure 40 bar, SOI 127 CAD BTDC.

(f) and temperature difference (ΔT) between the heat exchanger inlet and outlet.

As seen from Fig. 6, the required normalized heat $\overline{q}$ varies in the range of 18.2–19.4%. It is fair to assume that methanol conversion fraction (f) higher than 0.7 and ΔT lower than 50 K can be safely achieved. Moreover, since there are no special limitations on the heat exchanger (Fig. 3) design (i.e. no need in a catalyst, relatively low temperatures and flow rates of fluids whereas one side is liquid), we believe that ΔT in the range of 10–20 K is realistic. Thus, $\overline{q}$ will be around 18.5% with conversion fraction having only a minor effect on $\overline{q}$ – Fig. 6. The latter assessment makes sense because in the suggested configuration of the high-pressure TCR system where unreformed methanol and water are condensed in the heat exchanger – Fig. 3, the unreformed liquids cause parasitic losses only due to their temperature rise by ΔT. For this reason, the partial derivative $(\partial\overline{q}/\partial f)$ vanish for $\Delta T = 0$ and increases as ΔT increases – Eq. (15).

By using Eq. (16) and assuming that the exhaust gas leaves the reformer at 500 K, we calculated $\overline{h}_{av}$ as a function of λ and the exhaust gas temperature – Fig. 7. An assumption of the cooled exhaust temperature of 500 K was chosen. The latter was assumed to ensure that the temperature of the cooled hot stream (exhaust gas 8) is above the temperature of the heated cold stream (methanol–water mixture entering the reformer after pre-heating 2) and provides a sufficient temperature gradient for heat transfer – Fig. 3. We also plotted on Fig. 7 the experimental results obtained for WOT engine operation in the wide range of loads with λ varying from 1.55 to 4.2 (idle).

As seen in Fig. 7, at high load and $\lambda = 1.5$ the available enthalpy of the exhaust gas is sufficient to sustain the reforming reactions. As the load is decreased and excess air ratio is increased (at wide-open throttle) the amount of available enthalpy becomes marginal ($2 < \lambda < 2.5$) and then insufficient ($\lambda > 2.5$). Thus, the possibility of unthrottled operation at $\lambda > 2$ is dependent on the reforming system design characteristics such as ΔT, heat transfer losses through the system boundaries and the minimal possible exhaust gas temperature at the reformer outlet. The latter has a strong effect mainly at high excess air ratios because of the low exhaust gas temperatures and the relatively high flow rates at these operating modes. Considering the experimental point of $\lambda = 4.2$ and $T_{exh} = 540$ K as an example, the normalized available exhaust gas enthalpy $(\overline{h}_{av})$ is increased from 5.5% to 12.3% and 19.1% when the temperature of the cooled exhaust gas decreases from 500 K to 450 K and 400 K, respectively. In the considered case of the high-pressure TCR system, the exhaust gas temperature at the reformer outlet also depends on the reforming pressure. Lower reforming pressure will cause the water–methanol mixture to enter the reformer at a lower temperature due to partial evaporation at the pre-heating stage. Evaporation at the pre-heating stage becomes impossible with pressure increase. Hence, methanol–water temperature at the reformer inlet (2) increases and, as a result, the possible outlet temperature of exhaust gas increases as well. Engine operation at $\lambda > 2$ may be achieved by using a reformate reservoir which is filled while working at low excess air ratios or by delaying combustion through late ignition or

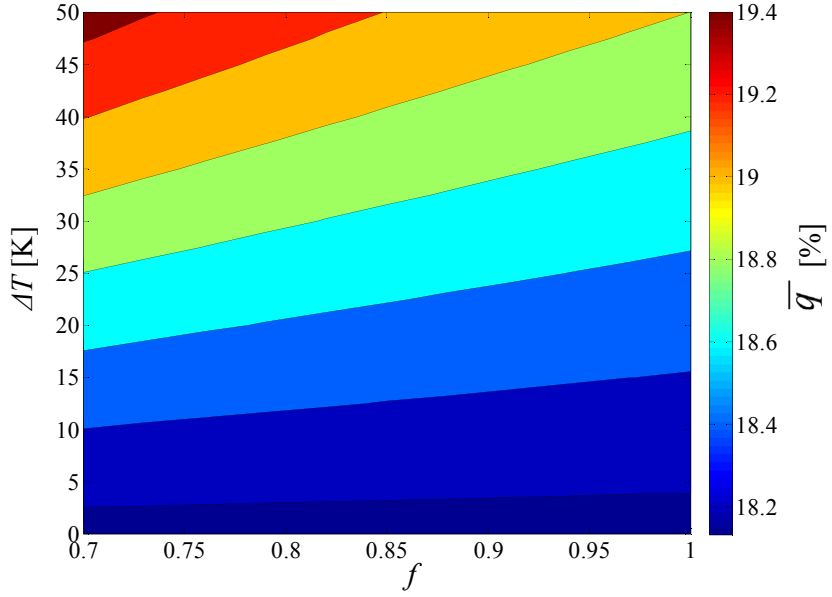

Fig. 6 – Percentage of the fuel energy delivered to the engine, which is required for reforming, as a function of the methanol conversion fraction (f) and the temperature difference (ΔT) between heat exchanger inlet (1) and outlet (4).

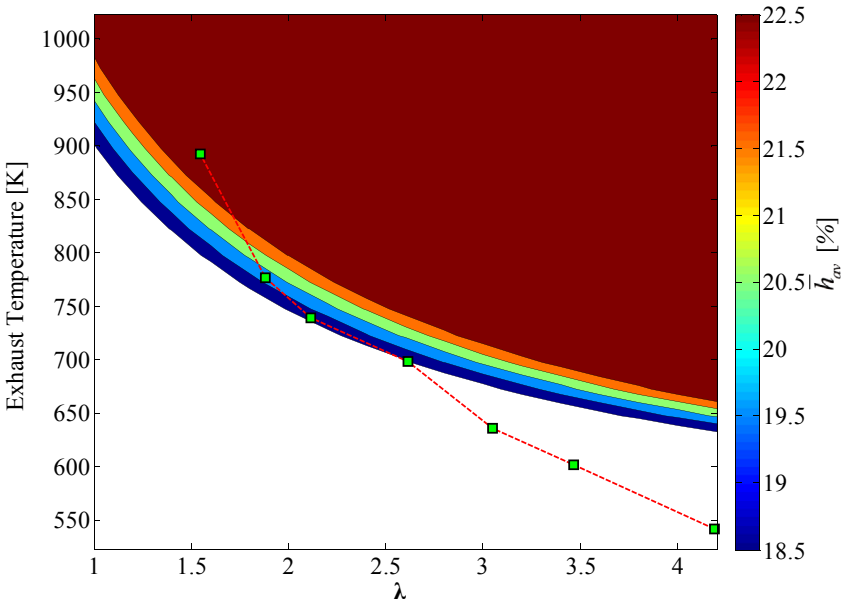

Fig. 7 – $\overline{h}_{av}$ as a function of λ and the exhaust gas temperature. Engine speed 2800 rpm; SOI 127 CAD BTDC; injection pressure at 40 bar; exhaust gas outlet temperature 500 K.

injection to increase exhaust gas temperatures. The effect of injection timing and pressure on engine efficiency and emissions was investigated and is discussed hereinafter.

It is clear that engine performance and emissions are dependent on the strategy of reformate injection, which affects the fuel–air mixing quality and thus influences combustion process. When a DI ICE with high-pressure TCR is considered, the injection pressure is a very important parameter because either the reformate has to be compressed prior to injection or the reforming has to be performed at high pressure [35,38]. Since compressing the reformate prior to its injection is an energy consuming process, it is beneficial to perform the reforming reactions at high pressure thus compressing the methanol and water at their liquid state and substantially reducing the energy required for compression. The drawbacks of high-pressure reforming are more severe requirements to the mechanical strength of the reforming system and a concern of catalyst deactivation due to coke formation. Another drawback of high-pressure reforming related to heat exchange process in the reformer and heat exchanger was discussed in the previous section. Thus, it is desirable to inject the fuel at the lowest possible injection pressure that allows sufficient reformate flow rate to meet engine power and efficiency requirements. It is important to remember that the required injection pressure is strongly influenced by the injector design and its fuel flow area. As the flow through the injector is choked during most of the injection period and at most of the injection pressures, the necessary injection pressure is inversely related to the injector flow area and injection period (Eq. (12)). An example presented in Fig. 8 for the engine operating mode at 2800 rpm, WOT and λ = 1.5 illustrates such a dependence and shows how the pressure required to allow sufficient fuel flow rate varies with the injection timing and injector flow area. The calculation

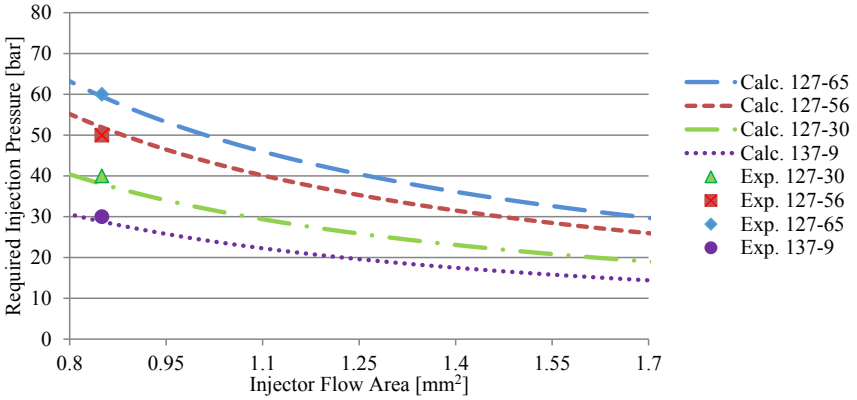

Fig. 8 – Required injection pressure as a function of the injection timing and the injector flow area. Engine speed 2800 rpm, WOT, λ = 1.5, C_D = 0.79, fuel mass per cycle 22.5 mg. Numbers in the legend: SOI-EOI CAD BTDC.

was based on the assumption of ideal gas flow (Eq. (12)) and experimentally obtained data for the same operating regime with the in-house developed injector (C_D = 0.79, A = 0.85 mm^2).

Since the injector is based on an available commercial injector, we tried to maximize the flow area by maximizing needle lift and concentric hole area to a degree that still allowed good sealing. Thus, we had no possibility to further increase the injector flow area. So, the parameters we varied in our experiments were injection pressure and injection timing only.

The injection pressure was varied from 30 to 60 bar and the SOI timing was varied from 137 to 97 CAD BTDC for WOT operation at an engine speed of 2800 rpm and excess air ratio of 1.5. The ignition timing was set as an MBT value (13 CAD BTDC) for the given speed and λ at injection pressure of 40 bar and SOI timing of 127 CAD BTDC. The ignition timing was kept constant in the studied range of injection timings and pressures due to limited amount of available MSR gas.

When the engine indicated efficiency values are plotted as a function of SOI timing and injection pressure, the indicated efficiency seems to be clearly dependent on the injection pressure (Fig. 9).

The lower engine efficiency in the case of the lower injection pressures (30 and 40 bar) and late SOI is a result of the late end of injection (EOI) that results in lower HRR and late end of combustion due to retarded mixing and late mixture formation (Fig. 10).

For the three cases shown in Fig. 10, the highest efficiency was achieved for early reformate injection at the higher pressure (blue line). In the latter case, injection ended early (65 CAD BTDC) allowing good fuel–air mixing before ignition. For this reason, the flame development angle (θ_{0-10}) was the lowest (10 CAD) in this case and only a relatively small fraction of the reformate was burned late in the expansion stroke (θ_{90} = 391 CAD). It also led to reduced cycle-to-cycle variation – Fig. 11. As SOI is retarded or the injection pressure is lowered, the end of injection is delayed allowing less time for mixture formation and thus causing an increase in the flame development angle (Fig. 10) and resulting in a higher fuel fraction that is burned late in the expansion stroke (θ_{90} = 417 CAD). Such a late and a slower combustion leads, as anticipated, to a more substantial cycle-to-cycle variation and is reflected in higher COV values – Fig. 11. In the shown cases (Fig. 10) the late high-pressure injection is more efficient than the early low-pressure injection because at 23 ATDC both cases has the

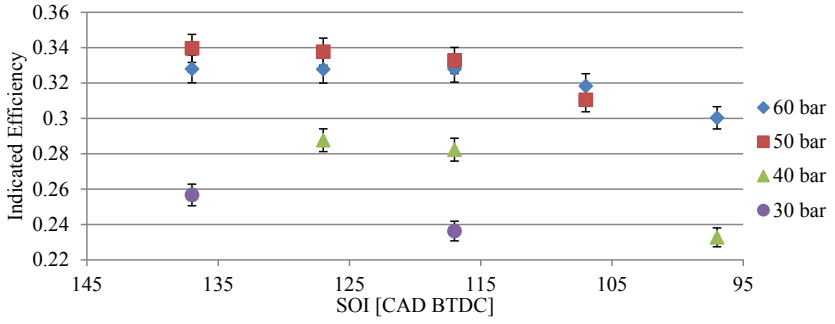

Fig. 9 – Indicated efficiency as a function of injection pressure and SOI timing. WOT, engine speed 2800 rpm and λ = 1.5. Error bars show the uncertainty of the calculated indicated efficiency values.

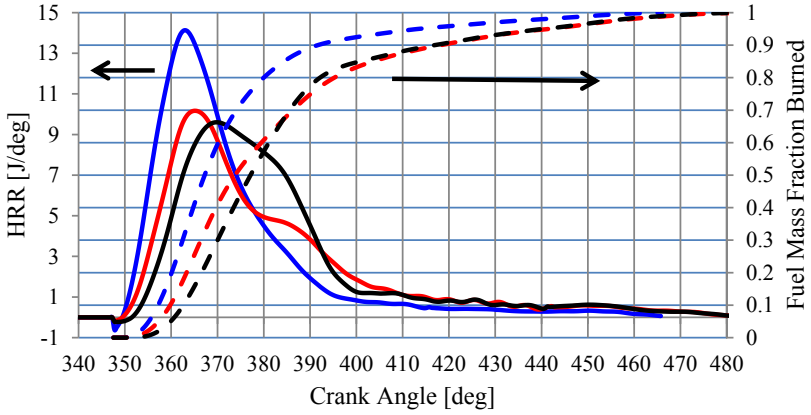

Fig. 10 – HRR and fuel mass fraction burned for 3 typical cases: injection period 117-23 CAD BTDC, 40 bar (red lines); injection period 117-54 CAD BTDC, 60 bar (blue lines); injection period 97-33 CAD BTDC, 60 bar (black lines). Engine speed 2800 rpm, WOT, λ = 1.5. Solid lines – HRR; dashed lines – fuel mass fraction burned. (For interpretation of the references to color in this figure legend, the reader is referred to the web version of this article.)

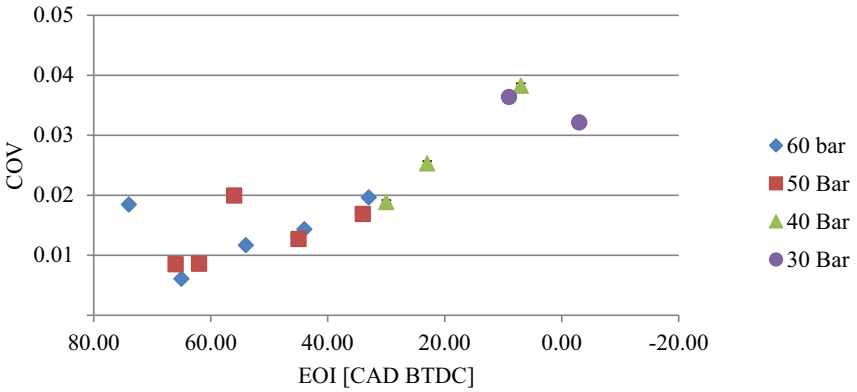

Fig. 11 – COV dependence on injection timing (EOI – end of injection). Error bars show the uncertainty of the calculated COV values.

same mass fraction burned, but for the low-pressure injection a higher portion of the fuel is burned later in the expansion stroke or too early BTDC. As can be seen from Fig. 10, for all the considered cases, the flame termination phase is relatively long due to the combustion chamber geometry of the tested engine (side-valve configuration).

Cycle-to-cycle variation is an important engine performance parameter because the optimum ignition timing is normally set for an average cycle [39]. Thus, for slow burning cycles the ignition is over-retarded and for fast burning cycles it is actually over-advanced resulting in loss of power and efficiency. Fast burning cycles lead to high in-cylinder pressure, high pressure rise rate, high NO_x formation and may also lead to knock appearance. These fast cycles limit the engine's compression ratio and affect a possibility of tuning optimization [39]. Cyclic variations in the cylinder are caused by mixture motion and excess air ratio variations especially in the vicinity of the spark plug, because they change the early flame development and thus affect the fuel burning behavior and the heat release rate. Hence, improved mixture formation leads to reduced cycle-to-cycle variations and has a beneficial effect on engine efficiency and emissions. As seen in Fig. 11, early EOI reduces the COV and hence has a beneficial effect on the efficiency. The data shown in Fig. 11 clearly indicate that cycle-to-cycle variation strongly depends on EOI timing, and hence the time available for fuel–air mixing, and almost insensitive to the injection pressure. When the end of injection is retarded from 65 towards 5 CAD BTDC, the obtained COV values rise from 1% to almost 4%, respectively.

Since the engine efficiency depends on injection timing through reformate-air mixture formation with the subsequent variation in COV and HRR, when we plot indicated efficiency vs. EOI, the different pressure lines of Fig. 9 almost merge into a single trend line (Fig. 12). This is explained by the mutual influence of the SOI timing and the injection pressure (which determines the flow rate through the injector and thus the injection duration) on the finally achieved end of injection. As expected, the late combustion resulted in higher available energy of exhaust gas (Fig. 12). The latter fact should be taken into account when an ICE with TCR is considered.

As seen in Fig. 12, if EOI is retarded beyond 50 CAD BTDC an increase in the available exhaust gas enthalpy ($\overline{h}_{av}$) and a sharp decrease in efficiency are observed, which is attributed to late combustion and increased cycle-to-cycle variation. The

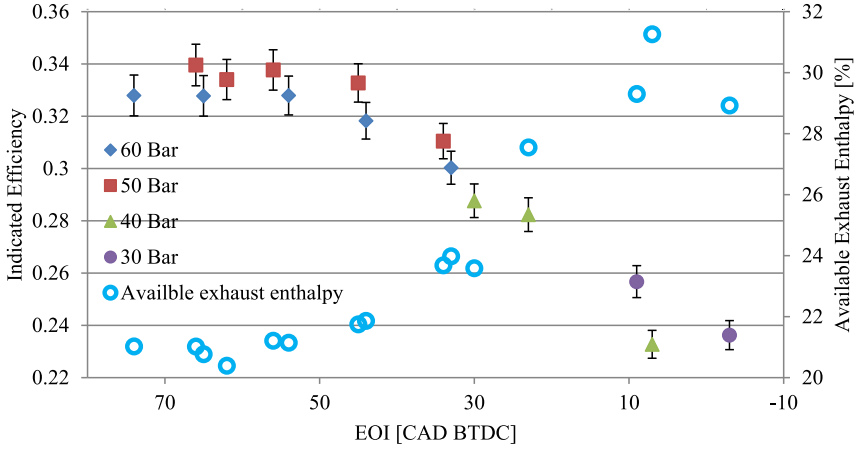

Fig. 12 – Indicated efficiency and available exhaust energy as a function of EOI timing and injection pressure. WOT, engine speed 2800 rpm and λ = 1.5. The temperature of the cooled exhaust gas assumed to be 500 K. Error bars show the uncertainty of the calculated indicated efficiency values.

efficiency decrease is observed at much earlier EOI values than reported in Ref. [45] where the performance of a DI ICE fed with pure hydrogen was studied. This finding may be addressed to the fact that in our case the baseline engine was not a DI engine and the process of reformate-air mixing within the cylinder was not optimized (this important task lies out of the scope of the reported research). The combustion chamber shape and the fact that the applied injector has a single injection axis, which was relatively far from the spark plug, delays mixture formation in the vicinity of the spark plug and leads to slower and delayed combustion. Another reason of the observed differences between the reformate and pure hydrogen combustion in a DI engine that in the case of methanol reformate combustion, the latter contains substantial amount (up to 25%) of a diluent gas CO_2. The higher specific heat of carbon dioxide compared to diluent air (by 5–8% in the temperature range 1000–2500 K) leads to combustion temperature reduction and, as a result, to lower burning velocities. Thus, the same EOI retarding results in a bigger combustion shift into the expansion stroke with the subsequent efficiency reduction.

A slight increase in efficiency as EOI is retarded was expected from previous simulations (carried out under assumption of negligible changes in mixing quality with EOI retarding) due to reduction of compression work (about 1.5% absolute improvement for 60 CAD retard for an engine with compression ratio of 10) [35]. The obtained experimental results show a possible appearance of a mild efficiency maximum (in the range of the uncertainty) as a function of EOI timing, which most probably reflects joint effect on efficiency of opposite influencing factors, like compression work, fuel–air mixing quality and combustion phasing. The experimental data show (Fig. 12) that for the studied conditions (engine speed 2800 rpm, $\lambda = 1.5$), the minimal reformate injection pressure, which is required to achieve the highest possible engine efficiency is 50 bar. It can be seen from Fig. 12 that if EOI could be advanced by 20 CAD (from approximately 30 towards 50 CAD BTDC), even injection pressure of 40 bar could be sufficient to achieve the highest possible efficiency. This would require SOI slightly before intake valve closing (IVC) and is possible, if backflow prevention could be achieved.

Similarly to engine efficiency, also pollutant emissions were found to be dependent mainly on EOI timing – Figs. 13–17. Specific emissions of various gaseous pollutants, as well as particle number concentrations, obtained at different injection pressures are almost merged into a single line when plotted vs EOI timing. This finding can be expected because CO_2 emissions are inversely related to engine efficiency; NO_x and CO – are related to the HRR and late combustion, which have been shown previously to be linked to EOI timing. Similarly to the indicated efficiency behavior, for all studied injection pressures, the pollutant emissions data merge into a single trend line. This implies that pollutant formation is mainly affected by the fuel–air mixing process. Figs. 13–16 show the CO_2, NO_x, CO and HC emissions as a function of the EOI, respectively.

CO_2 emissions (Fig. 13) show a possible appearance of a mild minimum at EOI timing of 50–60 CAD BTDC (in the range

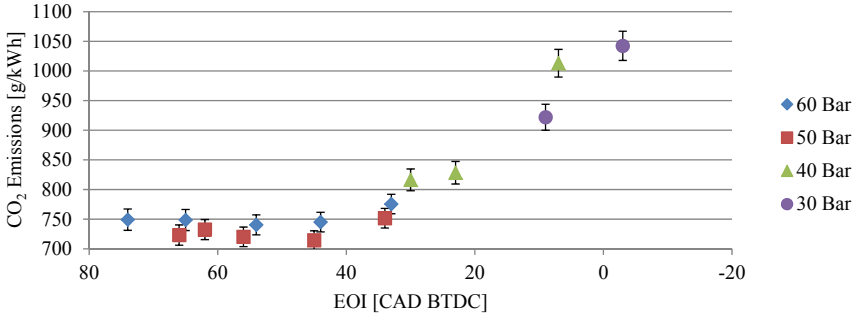

Fig. 13 – CO_2 emission as a function of EOI timing and injection pressure. WOT, engine speed 2800 rpm and $\lambda = 1.5$. Error bars show the uncertainty of the CO_2 emission values.

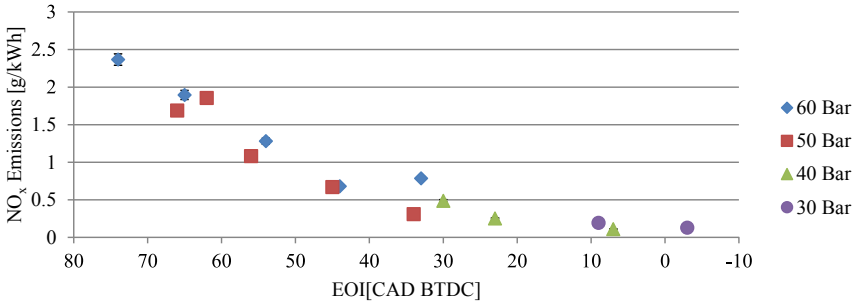

Fig. 14 – NO_x emission as a function of EOI timing and injection pressure. WOT, engine speed 2800 rpm and $\lambda = 1.5$. Error bars show the uncertainty of the NO_x emission values.

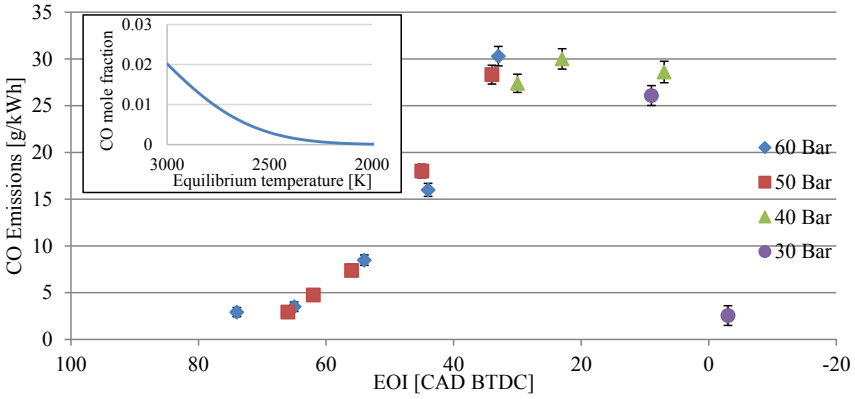

Fig. 15 – CO emission as a function of EOI timing and injection pressure. WOT, engine speed 2800 rpm and λ = 1.5. Error bars show the uncertainty of the CO emission values. Insert – CO equilibrium mole fraction vs temperature.

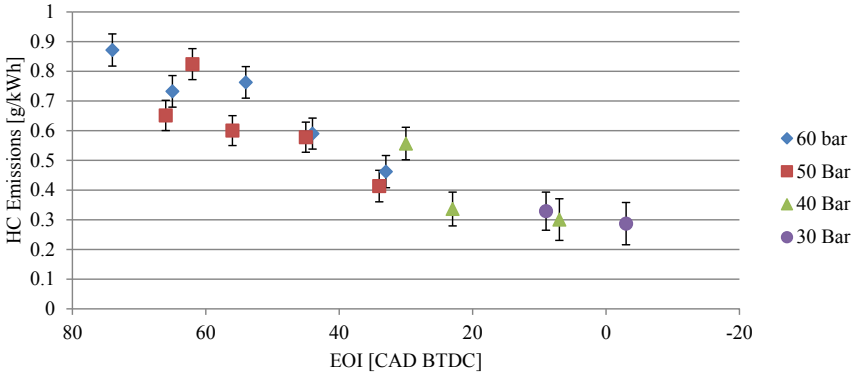

Fig. 16 – HC emission as a function of EOI timing and injection pressure. WOT, engine speed 2800 rpm and λ = 1.5. Error bars show the uncertainty of the HC emission values.

of the uncertainty) that matches the maximum of engine's efficiency.

As seen from Fig. 14, NO_x emissions decrease with EOI retarding due to late mixing and combustion that reduces in-cylinder temperatures. For some of the range it is at the cost of reduced efficiency but still there is a range between EOI of 74 and EOI of 50 CAD BTDC where indicated efficiency is almost constant and NO_x emissions drop by a factor of 2.5. This finding can be explained by the fact that at an advanced EOI timing compression work rise prevents increase in indicated efficiency, whereas high maximal in-cylinder temperatures lead to intensified NO_x formation. Another possible reason is linked to the ignition timing that was set at MBT value for the injection pressure of 40 bar and SOI timing of 127 CAD BTDC. For earlier EOIs with higher HHR, ignition was over-advanced thus resulting in higher temperatures and increased NO_x formation, but not higher efficiency.

As can be seen from Fig. 15, EOI retarding leads to significant increase in CO emissions. At some value of EOI timing (in our experiments at approximately 35 CAD BTDC) the measured levels of CO emission achieve a mild maximum and significantly decrease with further EOI retarding. The observed dependence of CO emission on EOI timing is defined by changes in chemical kinetics of CO_2 dissociation to CO affected by variations in combustion temperature and cooling rate. It is known that at high temperatures CO_2 dissociates to CO and the CO chemistry is assumed to be in equilibrium [39]. As the burned gas is cooled during the expansion stroke, CO mole fraction remains significantly higher than its equilibrium value due to the relatively slow kinetics. Furthermore, CO oxidation reactions are highly dependent on the cooling rate and actually freeze as the gas passes through the exhaust valves [39] and [46]. It is important to note that in the case of engine fueled with MSR reformate, CO_2 is introduced to the combustion process together with the fuel (hydrogen), and is not formed as a result of a hydrocarbon fuel combustion. In the considered case, as EOI is retarded, two opposing factors influence CO formation. First, the maximal combustion temperatures are decreased (which is reflected also in lower NO_x emissions with EOI retarding) leading to lower equilibrium CO concentrations – see the insert on Fig. 15 (equilibrium CO molar fractions were calculated for $p = 20$ bar and $\lambda = 1.5$ using [47,48]). Second, combustion is delayed, thus leading to higher temperatures later on in the expansion stroke. This can be clearly seen from the higher available exhaust gas enthalpy values with EOI retarding – Fig. 12. This leaves less time for CO oxidation before exhaust valve opening, reduces temperature relaxation time (increases cooling rate) and thus leads to

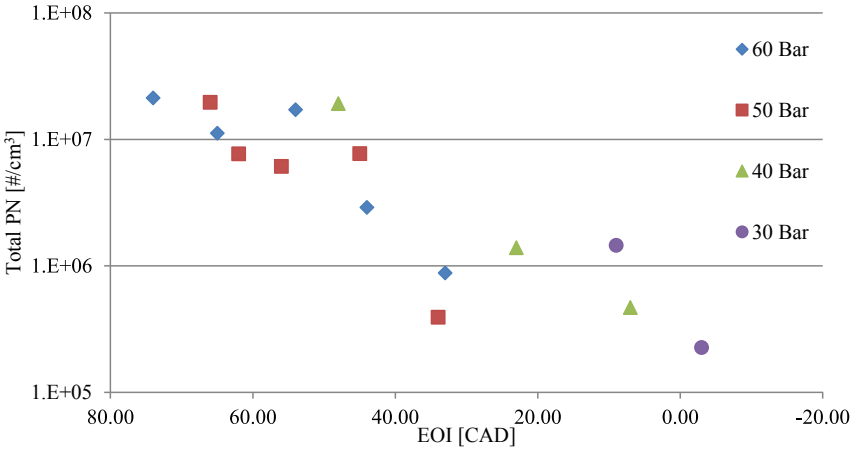

Fig. 17 – PN emission as a function of EOI timing and injection pressure. WOT, engine speed 2800 rpm and λ = 1.5.

higher CO emissions. We believe that as EOI is retarded from 75 to 35 CAD BTDC, the effect of increased cooling rate is more significant than the reduction of peak cylinder temperatures. This results in a rise of the measured CO emission. As EOI is further retarded, the effect of these phenomena becomes comparable, and with later EOI – the effect of temperature reduction begins to be dominant. This behavior is reflected in a mild maximum and a substantial reduction of CO emission that was measured at the most retarded EOI timing.

Dependence of HC emission on EOI timing is shown in Fig. 16. Since the only source for HC formation is lubrication oil [49], HC emissions decrease as combustion process is prolonged thus allowing completer oil combustion. The obtained results show a good potential of the DI engine with high-pressure TCR to achieve ultra-low emissions without any need in exhaust gas aftertreatment. In this case, a reformer will replace the currently used catalytic converter. However, further investigation of this subject is required to make definite conclusions about a possibility of engine operation without aftertreatment.

PN concentrations were much harder to measure due to the spiky nature of PN emission in SI engines [50]. This spiky nature was also observed in our measurements with spikes occurring every 30–60 s and spike duration between 5 and 20 s. Thus, it was decided to compare time-averaged PN emissions with measurements duration of at least 120 s at a measuring frequency 10 Hz. Even though the spiky nature of PN emission increases the measurement uncertainty, the trend of PN emission reduction with EOI retarding is clear (Fig. 17).

Although in the case of PN emission the scatter around the average emission line is higher than for other pollutants (notice the logarithmic scale) this may be due to the spiky nature of the PN emissions. The level of measured PN emissions is similar to that one observed earlier in Ref. [42] where particles formation in a hydrogen-fed ICE was investigated. Lubrication oil and deposits breakup are believed to be the source of PN emission. This explains the reduction in PN emission as the combustion is prolonged for retarded EOI timings. The latter, similarly to HC emission, allows more time for completer combustion of particles formed at earlier combustion stages. It is also possible that the lower temperatures at retarded EOI timing result in smaller amounts of burned lubricant and thus – lower HC and PN emissions.

Summary and conclusions

ICE feeding with MSR reformate allows a significant increase in ICE efficiency and a dramatic reduction in pollutant emissions compared with gasoline counterpart. That is due to the waste heat recovery and the favorable combustion properties of the hydrogen-rich reformate that allow fast combustion, lean-burn operation and lead to high HRR, reduced COV, lower in-cylinder temperatures and smaller throttling and heat transfer losses.

It was shown that although unthrottled engine operation with lean-burning is possible, the available enthalpy of exhaust gas for methanol reforming becomes marginal at $\lambda > 2$ and insufficient at $\lambda > 2.5$ for the suggested configuration of the high-pressure thermochemical recuperation system (Fig. 3) and at assumptions as were outlined earlier.

The experimental results show that for the studied conditions the minimal reformate injection pressure, which is required to achieve the highest possible engine efficiency is 50 bar. In the case that EOI could be advanced by 20 CAD (from approximately 30 towards 50 CAD BTDC), even injection pressure of 40 bar can be sufficient to achieve the highest possible efficiency. This would require SOI slightly before intake valve closing (IVC) and is possible, if backflow prevention could be achieved. Another possibility to reduce the required injection pressure is to increase the injector flow area.

The trends of reduction in NO_x, HC, PN emission and increase in CO emission were observed with EOI retarding. End-of-injection timing is shown to be the main influencing factor on engine efficiency and pollutant emissions. The obtained results indicate that there is a range of EOI timing where indicated efficiency is almost constant and NO_x emissions drop by a factor of 2.5. Particle number emissions can be reduced in this range by a factor of 4. Further

investigation on the nature of particles formation and size distribution in an engine fueled with MSR reformate is required.

Acknowledgments

The financial support of the Israel Science Foundation (grant 1728/12); Israel Ministry of Environmental Protection (grant 133-1-5); Israel Ministry of National Infrastructures, Energy and Water Resources (grant 215-11-025); Israel Ministry of Science, Technology and Space; Wolfson Family Charitable Trust; Rieger Foundation and Grand Technion Energy Program is gratefully acknowledged.

REFERENCES

[1] Bastani P, Heywood J, Hope C. The effect of uncertainty on US transport-related GHG emissions and fuel consumption out to 2050. Transp Res Part A 2012;46:517–48.
[2] Mironova EY, Lytkina AA, Ermilova MM, Efimov MN, Zemtsov LM, Orekhova NV, et al. Ethanol and methanol steam reforming on transition metal catalysts supported on detonation synthesis nanodiamonds for hydrogen production. Int J Hydrogen Energy 2015;40(8):3557–65.
[3] Wang X, Ge Y, Zhang C, Tan J, Hao L, Liu J, et al. Effects of engine misfire on regulated, unregulated emissions from a methanol-fueled vehicle and its ozone forming potential. Appl Energy 2016;177:187–95.
[4] Phongboonchoo Y, Thouchprasitchai N, Pongstabodee S. Hydrogen production with a low carbon monoxide content via methanol steam reforming over $Cu_xCe_yMg_z/Al_2O_3$ catalysts: optimization and stability. Int J Hydrogen Energy 2017;42(17):12220–35. http://dx.doi.org/10.1016/j.ijhydene.2017.03.112.
[5] Rivarolo M, Bellotti D, Magistri L, Massardo AF. Feasibility study of methanol production from different renewable sources and thermo-economic analysis. Int J Hydrogen Energy 2016;41(4):2105–16.
[6] Tartakovsky L, Baibikov V, Gutman M, Mosyak A, Veinblat M. Performance analysis of SI engine fueled by ethanol steam reforming products. SAE Technical Paper 2011-01-1992. 2011.
[7] Pearson RJ, Eisaman MD, Turner JWG, Edwards PP, Jiang Z, Kuznetsov VL, et al. Energy storage via carbon-neutral fuels made from CO_2, water, and renewable energy. Proc IEEE 2012;100(2):440–60.
[8] Liao CH, Horng RF. Investigation on the hydrogen production by methanol steam reforming with engine exhaust heat recovery strategy. Int J Hydrogen Energy 2016;41(9):4957–68.
[9] Chiriac R, Racovitza A, Podevin P, Descombes G. On the possibility to reduce CO_2 emissions of heat engines fuelled partially with hydrogen produced by waste heat recovery. Int J Hydrogen Energy 2015;40(45):15856–63.
[10] Tartakovsky L, Gutman M, Mosyak A. In: Santos Cavalcanti Emmanuel F, Barbosa Marcos Ribeiro, editors. Energy efficiency of road vehicles – trends and challenges. Chapter 3 in the edited collection "Energy efficiency: methods, limitations and challenges". Nova Science Publishers; 2012. p. 63–90.
[11] Chakravarthy VK, Daw CS, Pihl JA, Conklin JC. Study of the theoretical potential of thermochemical exhaust heat recuperation for internal combustion engines. Energy Fuels 2010;24(3):1529–37.
[12] Mohammed SEL, Baharom MB, Aziz ARA. Analysis of engine characteristics and emissions fueled by in-situ mixing of small amount of hydrogen in CNG. Int J Hydrogen Energy 2011;36(6):4029–37.
[13] Verhelst S. Recent progress in the use of hydrogen as a fuel for internal combustion engines. Int J Hydrogen Energy 2014;39:1071–85.
[14] Verhelst S, Wallner T. Hydrogen-fueled internal combustion engines. Prog Energy Combust Sci 2009;35:490–527.
[15] Morgenstern DA, Fornango JP. Low-temperature reforming of ethanol over copper-Plated Raney nickel: a new route to sustainable hydrogen for transportation. Energy Fuels 2005;19:1708–16.
[16] Wheeler JC, Stein RA, Morgenstern DA, Sall ED, Taylor JW. Low-temperature ethanol reforming: a multi-cylinder engine demonstration. SAE Technical Paper 2011-01-0142. 2011.
[17] Wijaya WY. Methanol steam reforming for hydrogen production: concept and evaluation of integrated advanced energy system [PhD thesis]. Tokyo, Japan: Tokyo Institute of Technology; 2013. p. 102.
[18] Poran A, Artoul M, Sheintuch M, Tartakovsky L. Modeling internal combustion engine with thermo-chemical recuperation of the waste heat by methanol steam reforming. SAE Int J Engines 2014;7:234–42.
[19] Twigg MV, Spencer MS. Deactivation of copper metal catalysts for methanol decomposition, methanol steam reforming and methanol synthesis. Top Catal 2003;22(3–4):191–203.
[20] Lu J, Li X, He S, Han C, Wan G, Lei Y, et al. Hydrogen production via methanol steam reforming over Ni-based catalysts: influences of Lanthanum (La) addition and supports. Int J Hydrogen Energy 2017;42(6):3647–57.
[21] Marbán G, López A, López I, Valdés-Solís T. A highly active, selective and stable copper/cobalt-structured nanocatalyst for methanol decomposition. Appl Catal B Environ 2010;99(1):257–64.
[22] Pettersson L, Sjostrom K. Decomposed methanol as a fuel—a review. Combust Sci Technol 1991;80(4–6):265–303.
[23] Matthias NS, Wallner T, Scarcelli R. A hydrogen direct injection engine concept that exceeds US DOE light-duty efficiency targets. SAE Int J Engines 2012;5:838–49.
[24] Gong C, Li D, Li Z, Liu F. Numerical study on combustion and emission in a DISI methanol engine with hydrogen addition. Int J Hydrogen Energy 2016;41(1):647–55.
[25] Hagos FY, Aziz ARA, Sulaiman SA. Syngas (H_2/CO) in a spark-ignition direct-injection engine. Part 1: combustion, performance and emissions comparison with CNG. Int J Hydrogen Energy 2014;39:17884–95.
[26] Hagos FY, Aziz ARA, Sulaiman SA. Investigation of deposit formation in direct-injection spark-ignition engine powered on syngas. Int J Automot Technol 2015;16(3):479–85.
[27] Hagos FY, Aziz ARA, Sulaiman SA, Firmansyah Mamat R. Effect of fuel injection timing of hydrogen rich syngas augmented with methane in direct-injection spark-ignition engine. Int J Hydrogen Energy 2017. http://dx.doi.org/10.1016/j.ijhydene.2017.03.091. in press.
[28] He Z, Gao Z, Zhu L, Li S, Li A, Zhang W, et al. Effects of H_2 and CO enrichment on the combustion, emission and performance characteristics of spark ignition natural gas engine. Fuel 2016;183:230–7.
[29] Omari A, Shapiro M, Tartakovsky L. Laminar burning velocity of alcohol steam reforming products and effects of cellularity on flame propagation. SAE Technical Paper 2015-01-0775. 2015.
[30] Ji C, Yang J, Liu X, Zhang B, Wang S, Gao B. A quasi-dimensional model for combustion performance prediction of an SI hydrogen-enriched methanol engine. Int J Hydrogen Energy 2016;41:17676–86.

[31] Li G, Zhang Z, You F, Pan Z, Zhang X, Dong J, et al. A novel strategy for hydrous-ethanol utilization: demonstration of a spark-ignition engine fueled with hydrogen-rich fuel from an onboard ethanol/steam reformer. Int J Hydrogen Energy 2013;38(14):5936–48.
[32] Shimada A, Ishikawa T. Improved thermal efficiency using hydrous ethanol reforming in SI engine. SAE Technical Paper 2013-24-0118. 2013.
[33] Tartakovsky L, Baibikov V, Veinblat M. Comparative performance analysis of SI engine fed by ethanol and methanol reforming products. SAE Technical Paper 2013-01-2617. 2013.
[34] Yoon HC, Otero J, Erickson PA. Reactor design limitations for the steam reforming of methanol. Appl Catal B Environ 2007;75(3):264–71.
[35] Poran A, Tartakovsky L. Energy efficiency of a direct-injection internal combustion engine with high-pressure methanol steam reforming. Energy 2015;88:506–14.
[36] Peppley BA, Amphlett JC, Kearns LM, Mann RF, Roberge PR. Hydrogen generation for fuel-cell power systems by high-pressure catalytic methanol-steam reforming. In: Proceedings of the energy conversion engineering conference, IECEC-97, 831-836; 1997. p. 831–6.
[37] Tartakovsky L, Amiel R, Baibikov V, Fleischman R, Gutman M, Poran A, et al. SI engine with direct injection of methanol reforming products – first experimental results. SAE Technical Paper 2015-32-0712. 2015.
[38] Poran A, Tartakovsky L. Performance and emissions of a direct injection internal combustion engine devised for joint operating with high-pressure thermochemical recuperation system. Energy 2017;124:214–26.
[39] Heywood JB. Internal combustion engine fundamentals. New York: McGraw-Hill; 1988.
[40] Lee K, Yoon M, Sunwoo M. A study on pegging methods for noisy cylinder pressure signal. Control Eng Pract 2008;16(8):922–9.
[41] Shavit A, Gutfinger C. Thermodynamics: from concepts to applications. Boca Raton: CRC Press; 2008.
[42] Moffat RJ. Describing the uncertainties in experimental results. Exp Therm Fluid Sci 1988;1(1):3–17.
[43] Brunt MF, Pond CR. Evaluation of techniques for absolute cylinder pressure correction. SAE Technical Paper 970036. 1997.
[44] Wang X, Grose MA, Caldow R, Osmondson BL, Swanson JJ, Chow JC, et al. Improvement of engine exhaust particle sizer (EEPS) size distribution measurement – II. Engine exhaust particles. J Aerosol Sci 2016;92:83–94.
[45] Mohammadi A, Shioji M, Nakai Y, Ishikura W, Tabo E. Performance and combustion characteristics of a direct injection SI hydrogen engine. Int J Hydrogen Energy 2007;32(2):296–304.
[46] Creighton JR. Dependence of CO emissions on the rate of product cooling. Combust Flame 2000;123(3):402–11.
[47] Turns SR. An introduction to combustion concepts and application. New York: McGraw–Hill; 2012.
[48] Olikara C, Borman GL. A computer program for calculating properties of equilibrium combustion products with some applications to IC engines. SAE Technical Paper 750468. 1975.
[49] Miller AL, Stipe CB, Habjan MC, Ahlstrand GG. Role of lubrication oil in particulate emissions from a hydrogen-powered internal combustion engine. Environ Sci Technol 2007;41(19):6828–35.
[50] Graskow BR, Kittelson DB, Abdul-Khalek IS, Ahmadi MR, Morris JE. Characterization of exhaust particulate emissions from a spark ignition engine. SAE technical paper 980528. 1998.